Journal of the European Ceramic Society 46 (2026) 117965

Contents lists available at ScienceDirect

Journal of the European Ceramic Society

journal homepage: www.elsevier.com/locate/jeurceramsoc

Acceptor and donor codoping of $SrTiO_3$: Impact on grain growth behavior, space charge and electrical properties

M. Pascal Zahler [a,*,1], Dylan Jennings [a,b,1,2], Olivier Guillon [a,c,d,3], Wolfgang Rheinheimer [a,d,1]

[a] Forschungszentrum Jülich GmbH, Institute of Energy Materials and Devices (IMD-2), Jülich 52425, Germany
[b] Ernst-Ruska Centre for Microscopy and Spectroscopy with Electrons (ER-C), Forschungszentrum Jülich, Jülich 52425, Germany
[c] Jülich Aachen Research Alliance: JARA-Energy, Jülich 52425, Germany
[d] RWTH Aachen University, Institute of Mineral Engineering, Aachen 52064, Germany

ARTICLE INFO

Keywords:
Co-doping
Strontium titanate
Solute drag
Microstructure
Grain growth
Electrochemical impedance spectroscopy
EDS-STEM
Grain boundary engineering

ABSTRACT

$SrTiO_3$ is a model electro-ceramic representing the very significant group of perovskite ceramics which display versatile electric properties (ferroelectricity, ionic conductivity, semi-conductivity). The impact of dopants on the properties of $SrTiO_3$ is comparably well investigated. This study explores the correlation between dopant type, grain growth and electrical properties of acceptor-donor codoped $SrTiO_3$. The electric properties of undoped and doped (Fe, Nb, Fe/Nb) $SrTiO_3$ were investigated using electrochemical impedance spectroscopy (EIS). Space charge potentials $\Delta\Phi$ and thickness λ_{MS} were evaluated. Cationic segregation profiles at grain boundaries (GBs) were characterized using Scanning Transmission Electron Microscopy (STEM) combined with Energy Dispersive X-ray Spectroscopy (EDS). Grain growth coefficients were evaluated for each sample. Fe segregation reduces grain growth rates (solute drag) and increases GB conductivity. Under certain annealing conditions solute drag transitions to abnormal grain growth. Codoping does not alter bulk conductivity. Nb doping drastically changes electric properties and grain growth kinetics.

1. Introduction

In ceramics, dopants are often used to engineer bulk properties which are often discussed within the framework of defect chemistry [1–3]. Yet, the impact of dopants on grain boundary (GB) properties and microstructure evolution is less understood than their impact on bulk properties.

$SrTiO_3$ is a well-known model material [4] for many other perovskite materials that are used in a variety of different electrical applications [5–8]. In many of these applications polycrystalline materials are used, and grain boundaries (GBs) have a detrimental effect on the overall performance of the material. The low GB conductivity of perovskites such as $SrTiO_3$ is caused by space charge layers at the GBs [9–12], which form due to the preferential formation of oxygen vacancies ($V_O^{\cdot\cdot}$) in the GB core. The GB core charge leads to the segregation and depletion of other point defects at the GB forming a potential barrier, the space charge potential ($\Delta\Phi$) [13–15]. The composition of the space charge layer as well as the strength of the $\Delta\Phi$ are determined by the bulk's defect chemistry [12,16].

Besides impacting the electrical properties of a polycrystalline ceramic, segregation and space charge can also impact the microstructural evolution of a polycrystal. Segregated cations at GBs can both decrease [17–19] or increase [18,20,21] the grain growth kinetics which changes the GB density and by that the overall contribution of GBs to the total conductivity of a system [22]. The often slow diffusion rates of segregated cations inhibit the migration rate of GBs; this effect is known as solute drag [23–26] which is suspected to cause abnormal grain growth (AGG) [27–29]. Note that many other causes for abnormal grain growth exist such as nucleation barriers [30–32], GB anisotropy [33–36], intergranular glass films [17,37] or complexions [21,38,39]. AGG is known to occur in many perovskite materials such as $SrTiO_3$ [40], $BaTiO_3$ [41], $(KNa)_{0.5}NbO_3$ [32,42] and $Li_{0.5}La_{0.5}TiO_3$ [40]. The

* Corresponding author.
E-mail address: pascal.zahler@ikmt.uni-stuttgart.de (M.P. Zahler).
[1] Now at Institute for Ceramic Materials and Technologies (IKMT), Stuttgart University, 70569 Stuttgart, Germany
[2] Now at Faculty of Physics and Astronomy, Advanced Transmission Electron Microscopy, Ruhr University Bochum, 44801 Bochum, Germany
[3] Currently at Luxembourg Institute of Science and Technology, 4362 Esch-sur-Alzette, Luxembourg

https://doi.org/10.1016/j.jeurceramsoc.2025.117965
Received 24 July 2025; Received in revised form 21 October 2025; Accepted 5 November 2025
Available online 6 November 2025
0955-2219/© 2025 The Author(s). Published by Elsevier Ltd. This is an open access article under the CC BY license (http://creativecommons.org/licenses/by/4.0/).

AGG in $SrTiO_3$ leads to non-Arrhenius grain growth behavior, where the grain growth rate decreases by orders of magnitude within a transition temperature range [43,44]. This behavior is proposed to be caused by the presence of two grain boundary populations with different compositions and migration rates, i.e. different solute drag behaviors [15,36,45]. In the transition temperature range, the dominating GB population changes from one to the other, also impacting the electric properties [46].

There has been extensive work on the impact of dopants on the electric properties of bulk [3,47–51], electric properties of the GBs [52–56] and grain growth kinetics [27,30,31,57]; yet many studies investigate these properties or mechanisms separately from one another. To achieve a full picture and to be able to properly design a material, the interconnection of these effects has to be understood. Dopants have to be carefully selected and combined to achieve desired electrical properties and microstructures.

In this study, the impact of acceptor, donor and acceptor-donor co-doping on the electric properties of $SrTiO_3$ ceramics and its grain growth behavior is investigated. Undoped, Fe-doped, Nb-doped and Nb/Fe codoped $SrTiO_3$ are prepared. Dopants were chosen based on their impact on $SrTiO_3$'s defect chemistry and how they segregate towards grain boundaries. Fe is an acceptor dopant that increases the oxygen vacancy concentration $[V_O^{\cdot\cdot}]$, increases the electron hole concentration p [1,4,58], segregates at GBs [9,15,59] and slows down grain growth rates [19,26,28]. Nb is a donor dopant that reduces $[V_O^{\cdot\cdot}]$ while increasing $[V_{Sr}^{\cdot\cdot}]$ and the concentration of free electrons n [1,3,60,61]. Nb/Fe co-doping should not introduce any additional point defect besides Fe'_{Ti} and $Nb^{\cdot}_{Ti}$ to the material because Nb and Fe should charge-compensate each other if present in the same concentration [62–64]. GBs are investigated using scanning transmission electron microscopy (STEM) and electrochemical impedance spectroscopy (EIS). Grain growth kinetics of doped samples were determined. Fe doping leads to Fe segregation at GB and an increase in GB conductivity. Samples containing Fe show clear signs of solute drag. Purely Nb-doped samples exhibits a grain growth behavior deviating from undoped $SrTiO_3$. Results are discussed within the framework of defect chemistry, space charge and solute drag.

2. Experimental procedure

2.1. Powder processing

Undoped ($SrTiO_3$), Fe-doped ($SrTi_{0.98}Fe_{0.02}O_{3-\delta}$), Nb-doped ($SrTi_{0.98}Nb_{0.02}O_3$) and Nb/Fe codoped ($SrTi_{0.98}Nb_{0.01}Fe_{0.01}O_3$) strontium titante powder was synthesized by the mixed oxide/carbonate route. TiO_2 (≥99.9 %, Merck), $SrCO_3$ (≥99.9 %, Merck), Fe_2O_3 (>99 %, Alfa Aesar) and Nb_2O_5 (≥99.9 %, Merck) were used as raw powders. The powders were milled in a ZrO_2 crucible with 3 mm ZrO_2 milling balls (Tosoh, Japan) and isopropanol (Sigma-Aldrich) using a PM400 planetary ball mill (Retsch, Germany). After the first milling step, the powder suspension was dried. The dried powder was then sieved with a 150 μm mesh and calcined at 975 °C for 3 h in air. After calcination the powder was again milled to break any agglomerates that might have formed during calcination.

The phase purity of the powder was analyzed using x-ray diffraction (XRD) method. The XRD pattern were measured by with a D4 Endeavor (Bruker, Germany) X-ray diffractometer. The XRD data can be found in the supplementary information (see Figure S1).

2.2. Microstructure evolution

Green bodies were fabricated by uniaxial pressing the as synthesized powders in a die with a diameter of 10 mm using a pressure of 6 MPa. Stearic acid was used as lubricant during pressing. Cold-isostatic pressing at 400 MPa for 2 min was utilized to further densify the green bodies before sintering. As-prepared green bodies were pre-sintered to achieve homogeneous and dense microstructure that could be used for grain growth experiments. Undoped $SrTiO_3$ was pre-sintered at 1425 °C for 1 h, Fe-doped $SrTiO_3$ was pre-sintered at 1350 °C for 1 h and at Fe/Nb codoped $SrTiO_3$ was pre-sintered at 1375 °C for 1 h. Nb-doped samples were not pre-sintered since no satisfying density could be achieved. In the case of undoped and Fe-doped $SrTiO_3$ data from previous grain growth studies were used for comparison [19,43]. Impedance samples of undoped and Fe doped sample were obtained by annealing pre-sintered samples at 1350 °C for 10 h. The annealing conditions of undoped, Fe-doped and Nb/Fe codoped are listed in Table 1. Nb-doped samples were sintered using the same parameters used to anneal Nb/Fe doped samples. Heating and cooling rates for the sintering and annealing experiments were adjusted to 10 K/min.

2.3. Microstructure characterization

Microstructures of the sintered ceramics were investigated using a Zeiss Evo 15 SEM (Zeiss, Germany). If present, secondary phases inside the microstructures were investigated using Energy Dispersive X-ray Spectroscopy (SEM-EDS). The line intercept method was used to evaluate the average grain sizes of the samples. The standard error on the mean was calculated for each grain size. If samples featured bimodal microstructures, average grain sizes of the normal and abnormal grains were determined separately. Grain growth coefficients were obtained by fitting grain growth models to the average grain sizes plotted versus the annealing time. Grain size data of unimodal microstructures were fitted with Eq. 1 [65].

$$D^2 - D_0^2 = k \cdot t \tag{1}$$

Here, D is the average grain size after time t, k is the grain growth coefficient and D_0 is the initial average grain size at time $t = 0$.

For determining the grain growth coefficients of abnormal grains, a more sophisticated model has to be utilized. Eq. 1 assumes that every grain has the same driving force for grain growth (i.e. $\propto D^{-1}$), yet abnormal grains have a higher driving force for grain growth than normal grains, resulting in an overestimation of the abnormal grains' grain growth coefficient. Rheinheimer et al. used a different approach where abnormal grains are treated as single crystals growing into a polycrystalline matrix of small grains [43] (see Eq. 2).

$$D_{AGG}(t) = 6 \cdot \frac{k_{AGG}}{k_{NGG}} \left[\sqrt{k_{NGG} \cdot t + D_{NGG,0}^2} - D_{AGG,0} \right] + D_{AGG,0} \tag{2}$$

Table 1
Annealing temperatures and times for undoped, Fe-doped and Nb/Fe codoped $SrTiO_3$ samples. The sintering temperatures of Nb-doped $SrTiO_3$ are also included.

Temperature (°C)	Time (h)			
	Undoped [43]	Fe doped [19]	Nb doped	Nb/Fe doped
1300	0.5, 2, 5, 10 h	2, 10, 20 h	-	-
1350	0.5, 2, 5, **10 h**	1, 4, **10,** 20 h	5, 10, 20 h	5, 10, 20 h
1370	-	-	5, 10, 20 h	5, 10, 20 h
1400	0.5, 2, 5, 10 h	-	2, 5, 10 h	2, 5, 10 h
1425	0.5, 2, 5, 10 h	1, 4, 20 h	2, 5, 10 h	2, 5, 10 h
1450	-	-	2, 5, 10 h	2, 5, 10 h
1460	-	0.5, 1, 2 h	-	-
1475	-	-	1, 2, 5 h	1, 2, 5 h
1500	0.5, 2, 5, 10 h	-	1, 2, 5 h	1, 2, 5 h
1600	0.5, 2, 5, 10 h	-	0.5, 1, 2 h	0.5, 1, 2 h

Note that the different annealing conditions were chosen to accommodate for the different grain growth kinetics of the materials. Short annealing times were chosen for fast grain growth kinetics and long annealing times for slow grain growth kinetics. Densities of undoped, Fe-doped, Nb-doped and Nb/Fe codoped $SrTiO_3$ were determined by Archimedes method after sintering.

Here, $D_{AGG}(t)$ is the grain size of the abnormal grains after annealing time t for a given temperature, k_{AGG} is the grain growth coefficient of the abnormal grains, k_{NGG} is the grain growth coefficient of the normal grains, $D_{NGG,0}$ is the initial grain size of the normal grains and $D_{AGG,0}$ is the initial grain size of the abnormal grains. $D_{NGG,0}$ and $D_{AGG,0}$ are assumed to be the same in this study, and k_{NGG} is determined using Eq. 1.

2.4. GB characterization

A Hitachi HF5000 S/TEM was utilized for characterization the composition of general GBs in undoped and doped $SrTiO_3$ samples. High Angle Annular Dark Field (HAADF) images and Energy Dispersive X-ray Spectroscopy (EDS) maps were made at the grain boundaries of these samples. Post-analysis of the EDS data was performed with Hyperspy [66]. EDS maps and EDS line scans were quantified using a standardless (Cliff-Lorimer) quantification. Selected STEM samples were prepared using a Thermo Fisher Scientific Helios 460F1 FIB-SEM. Additional STEM samples were made by a conventional dimpling and ion milling process, utilizing a Gatan PIPS II. The Gibbsian GB excess of cationic species was determined according to [67–69]. The detection limit of the grain boundary excess measurements (following the procedure of Sternlicht et al. [68]) was determined for each element based on the average of all measurements done for said element. The probe diameter during EDS measurements is estimated to have been below 140 pm.

2.5. Electrochemical impedance analysis and space charge layer characterization

Impedance samples were ground to the desired thickness of 2 mm using SiC grinding paper with a mesh of 1200. Afterwards samples were contacted using Pt paste which was burned onto the samples at 900 °C for 2 h. An Alpha-A high frequency analyzer (Novocontrol Technologies GmbH & Co. KG, Germany) was utilized for electrochemical analysis of $SrTiO_3$ samples. Measurements were performed between 600 °C and 400 °C in a frequency range of 10 MHz to 100 mHz. The heating rate was set to 5 K/min and measurements were performed at temperature steps of 12.5 K. Impedance data were analyzed using the RelaxIS software (rhd instruments, Germany). Impedance data were fitted using equivalent circuits designed based on the brick-layer model [70–72]. The equivalent circuits consisted of a series of multiple RQ-circuits (resistor and constant phase element in parallel). The number of RQ-circuits depended on the sample composition. In the case of undoped and Nb/Fe codoped $SrTiO_3$, three RQ-circuits represented the bulk and two GB responses. The impedance response of the sample-electrode interfaces was often too small to be visible and only present in the very low frequency part of the impedance. Fe-doped samples were also fitted using 3RQ circuits, where one represents the bulk, another the GB and the third the electrode-sample interface. In the case of Nb-doped samples, a small electric resistance of 3 Ω to 10 Ω left of the high frequency part of the impedance plots was identified. The electrical resistance most likely stems from the Pt wires used to connect the sample electronically. Accordingly, the impedance response of Nb-doped $SrTiO_3$ was fitted with two RQ-circuits in series with a single resistor. One of the RQ-circuits represents the sample-electrode interface while the other RQ-circuit contains the impedance response of both bulk and GB. Bulk and GB contributions were separated from one another based on their capacity values. Bulk conductivity was calculated using Eq. 3 [73].

$$\sigma_{bulk} = \frac{1}{R_{bulk}} \cdot \frac{l}{A} \tag{3}$$

Here, R_{bulk} is the resistance of the bulk, l is the sample's thickness and A is the cross-sectional area of the electrodes and samples. The GBs' specific conductivity was calculated according to Eq. 4 [52], where C_{bulk} and C_{GB} are the total capacities of the bulk and GBs, respectively.

$$\sigma_{GB} = \frac{1}{R_{GB}} \cdot \frac{l}{A} \cdot \frac{C_{bulk}}{C_{GB}} \tag{4}$$

Space charge potentials (Eq. 6) and thicknesses (Eq. 9) were evaluated according to the Mott-Schottky model [9,22,74,75].

If the GB impedance consisted of two signals the average specific GB conductivity was evaluated according to Eq. 5.

$$\sigma_{GB,Avg.} = \frac{1}{(R_{GB,1} + R_{GB,2})} \cdot \frac{l}{A} \cdot C_{bulk} \left(\frac{1}{C_{GB,1}} + \frac{1}{C_{GB,2}}\right) \tag{5}$$

Here $R_{GB,1}$, $R_{GB,2}$, $C_{GB,1}$ and $C_{GB,2}$ are the resistance and capacitance values of the two GB impedance signals respectively. The space charge potential $\Delta\Phi$ is obtained by numerically solving Eq. 6, where τ_{GB} and τ_{Bulk} are the relaxation times of GB and bulk respectively, z_{mobile} is the charge number of the mobile defect, F is the Faraday constant, R is gas constant and T the temperature in K.

$$\frac{\tau_{GB}}{\tau_{bulk}} = \frac{\exp\left(\frac{z_{mobile} F \Delta\Phi}{RT}\right)}{2 z_{mobile} F \Delta\Phi} \cdot RT \tag{6}$$

For calculating the space charge thickness λ_{MS} the Debye layer thickness λ_{debye} is required which is equivalent to the space charge thickness predicted by the Gouy-Chapman model [16,74,75].

$$\lambda_{Debye} = \sqrt{\frac{\epsilon_0 \epsilon_r k_B T}{2 z_{major}^2 F^2 \cdot c_{major}}} \tag{7}$$

Where ϵ_0 is the permittivity of the vacuum, ϵ_r is the relative permittivity of $SrTiO_3$, z_{major} is the charge number of the major defect and c_{major} is the concentration of the majority defect. For every sample characterized in this study, the majority defects are cationic impurities or the doping species. Other defects such as $V_O^{\cdot\cdot}$, $h^{\cdot}$ or n' are always present at lower concentrations for the experimental conditions used in this study. The permittivity of $SrTiO_3$ is determined according to Eq. 8 [76] where C is 91900 K (± 2.7 %).

$$\epsilon_r = \frac{C}{T} \tag{8}$$

The space charge thickness λ_{MS} is evaluated by solving Eq. 9 using the results of Eq. 6 and Eq. 7.

$$\lambda_{MS} = \lambda_{Debye} \cdot \sqrt{\frac{4 z_{mobile} \Delta\Phi}{k_B T}} \tag{9}$$

Whether or not a defect is mobile depends on its diffusion coefficient or defect mobility, the temperature and the oxygen partial pressure. Electrons and electron holes are always mobile defects, while ionic defects only are mobile above a certain temperature.

For donor doped $SrTiO_3$, it is generally accepted that the compensation mechanism is primarily electric for reducing atmospheres. The donors $D_{Ti}^{\cdot}$ are compensated by electrons e' with their concentration being $n \approx [D_{Ti}^{\cdot}]$ [3]. At higher $P(O_2)$, strontium vacancies start to compensate the donor dopants [1,3,47], but are not mobile below temperatures of around 1000 °C [50,77,78]. For that reason, the mobile defects present in donor doped $SrTiO_3$ were considered to be e'.

In undoped and acceptor doped $SrTiO_3$, the acceptors A' are mainly compensated by ionic defects (i.e. $V_O^{\cdot\cdot}$). At intermediate and slightly oxidizing $P(O_2)$, the oxygen vacancy concentration $[V_O^{\cdot\cdot}]$ is fixed by the acceptor concentration. In more oxidizing atmosphere, electron holes $h^{\cdot}$ also compensate A' [3,79]. For that reason, acceptor doped $SrTiO_3$ can be a mixed conductor of oxygen vacancies $V_O^{\cdot\cdot}$ and electron holes $h^{\cdot}$ in the right conditions (T and $P(O_2)$) [11]. For the measurement conditions used in this study (< 600 °C in air), acceptor and undoped $SrTiO_3$ are known to be mainly p-type $h^{\cdot}$ conductors [58]. $h^{\cdot}$ were assumed to be the mobile defects in this study instead of $V_O^{\cdot\cdot}$. The same is true for Nb/Fe

codoped $SrTiO_3$ ceramics: Since $[Fe'_{Ti}] \approx [Nb^{\cdot}_{Ti}]$, it is expected that acceptors and donors compensate each other. For that reason, $[V^{\cdot\cdot}_O]$ and p of Nb/Fe codoped $SrTiO_3$ are expected to be the same as that of undoped $SrTiO_3$ because $V^{\cdot\cdot}_O$ and $h^{\cdot}$ can only be introduced from natural impurities.

For the calculation of the space charge layer width, the concentration of the majority defect is needed. $[A'_{Ti}]$ was assume to be $1{\cdot}10^{24}$ cm^{-3} for undoped $SrTiO_3$ [4] and $3.37{\cdot}10^{26}$ cm^{-3} for Fe-doped $SrTiO_3$. The donor concentration $[D^{\cdot}_{Ti}]$ was assumed to be $3.37{\cdot}10^{26}$ cm^{-3} for Nb-doped $SrTiO_3$. The majority defect concentration in Nb/Fe codoped $SrTiO_3$ was set to be the same as either the donor or acceptor concentration; with $[Fe'_{Ti}] = [Nb^{\cdot}_{Ti}] \approx 1.69{\cdot}10^{26}$ cm^{-3}.

3. Results

3.1. Sintering and microstructure evolution

The relative density of undoped, Fe-doped and Nb/Fe codoped $SrTiO_3$ range between 99.1 % and 99.7 % after pre-sintering. A variety of sintering conditions were tested for Nb-doped $SrTiO_3$ yet the density data featured significant variation (96–99 %).

Grain growth rates of normal and abnormal grains (k_{NGG} and k_{AGG}) in Fe-doped, Nb-doped and Nb/Fe codoped $SrTiO_3$ are shown in Fig. 1. The grain growth coefficient of normal grains in Fe-doped $SrTiO_3$ and of slowly-growing grains in undoped $SrTiO_3$ follow similar slopes with temperature. Grain growth coefficients of abnormal grains in Fe-doped $SrTiO_3$ are one to two orders of magnitude higher than those of normal grains which barely grow at all at lower temperatures (<1425 °C).

BSE-SEM images of Nb doped and Nb/Fe codoped microstructures are shown in Fig. 2 and Fig. 3 (Figure S2 and Figure S3 show additional microstructures). A list of the corresponding grain sizes for normal and abnormal grain populations are included in the supplementary part (Table S2 and Table S3).

Nb-doped $SrTiO_3$ features normal grain growth with unimodal microstructures at 1350 °C and 1370 °C (Fig. 2). The grain growth coefficient of Nb-doped $SrTiO_3$ is about one order of magnitude lower than that of the undoped $SrTiO_3$ (Fig. 1). At temperatures of 1400 °C and above, abnormal grain growth (indicated by bimodal microstructures) is observed (Fig. 2c-f). The grain growth rate of abnormal grains is only two to four times higher than that of normal grains. The slope of the grain growth rate also seems to decrease at 1400 °C. Grain growth stagnation is observed in Nb doped $SrTiO_3$ for some of the annealing conditions (see supplementary Figure S2 and Table S3). It has also been observed, that both grain size in Nb-doped $SrTiO_3$ is linearly correlated to the square root of porosity (Figure S6). This correlation indicates pore coarsening or swelling of closed pores.

Nb/Fe codoped samples annealed at 1350 °C or 1370 °C feature unimodal microstructures for all annealing times (Fig. 3). Nb/Fe codoped samples annealed at higher temperatures feature abnormal grain growth (bimodal microstructures, Fig. 3c-f). Mostly abnormal grains remain at 1500 °C after 5 h and at 1600 °C for any annealing time microstructures could again be regarded as unimodal. Normal grains grow significantly slower than the abnormal grains in Nb/Fe codoped $SrTiO_3$ which is reflected in the grain growth coefficients of both grain populations depicted in Fig. 1. The normal grains in Nb/Fe codoped $SrTiO_3$ have similar grain growth coefficients to the small grains in Fe doped $SrTiO_3$. The abnormal grains in Nb/Fe codoped $SrTiO_3$ have comparable growth rates to abnormal grains in undoped $SrTiO_3$.

3.2. Electrical characterization

The electrical properties of undoped, Fe doped, Nb doped and Nb/Fe codoped $SrTiO_3$ annealed at 1350 °C for 10 h, and 1500 °C for 2 h were investigated by EIS. The microstructures annealed at these temperatures were still unimodal. This is important because the microstructure can influence the GBs' impedance signal [80]. Nyquist impedance plots are shown in Fig. 4; semi-circles representing the bulk, grain boundary and electrode signal were added for better visualization. BSE-SEM images of the corresponding microstructures were added to the supplementary information (Figure S6). A direct comparison of the impedance plots is also shown in the supplementary section (Figure S5).

Undoped $SrTiO_3$ features a large distorted GB semi-circle that had to be fitted using two RQ-circuits both representing the GBs in the materials [46]. Similarly, the GB impedance of Nb/Fe codoped $SrTiO_3$ was fitted with two RQ-circuits. It was previously reported that the bulk and grain boundary impedance of Nb doped $SrTiO_3$ are hard to distinguish and micro-impedance measurements at single GBs are necessary to identify the grain boundary impedance [81–83]. This was also true in the current study where no separation of bulk and GB impedance of Nb doped $SrTiO_3$ was possible.

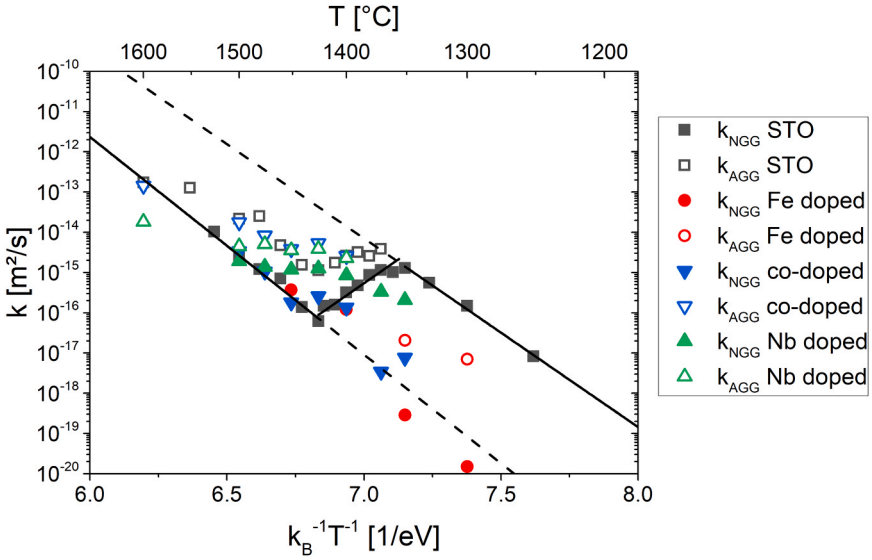


Fig. 1. Arrhenius-plots of the grain growth coefficients of undoped [43], Fe-doped $SrTiO_3$ [19], Nb-doped $SrTiO_3$ and Nb/Fe codoped $SrTiO_3$. Grain growth coefficients of normal and abnormal grains are plotted separately. k_{NGG} and k_{AGG} represent the grain growth coefficient of normal and abnormal grain growth in the respective materials. The error bars were smaller than the corresponding symbols.

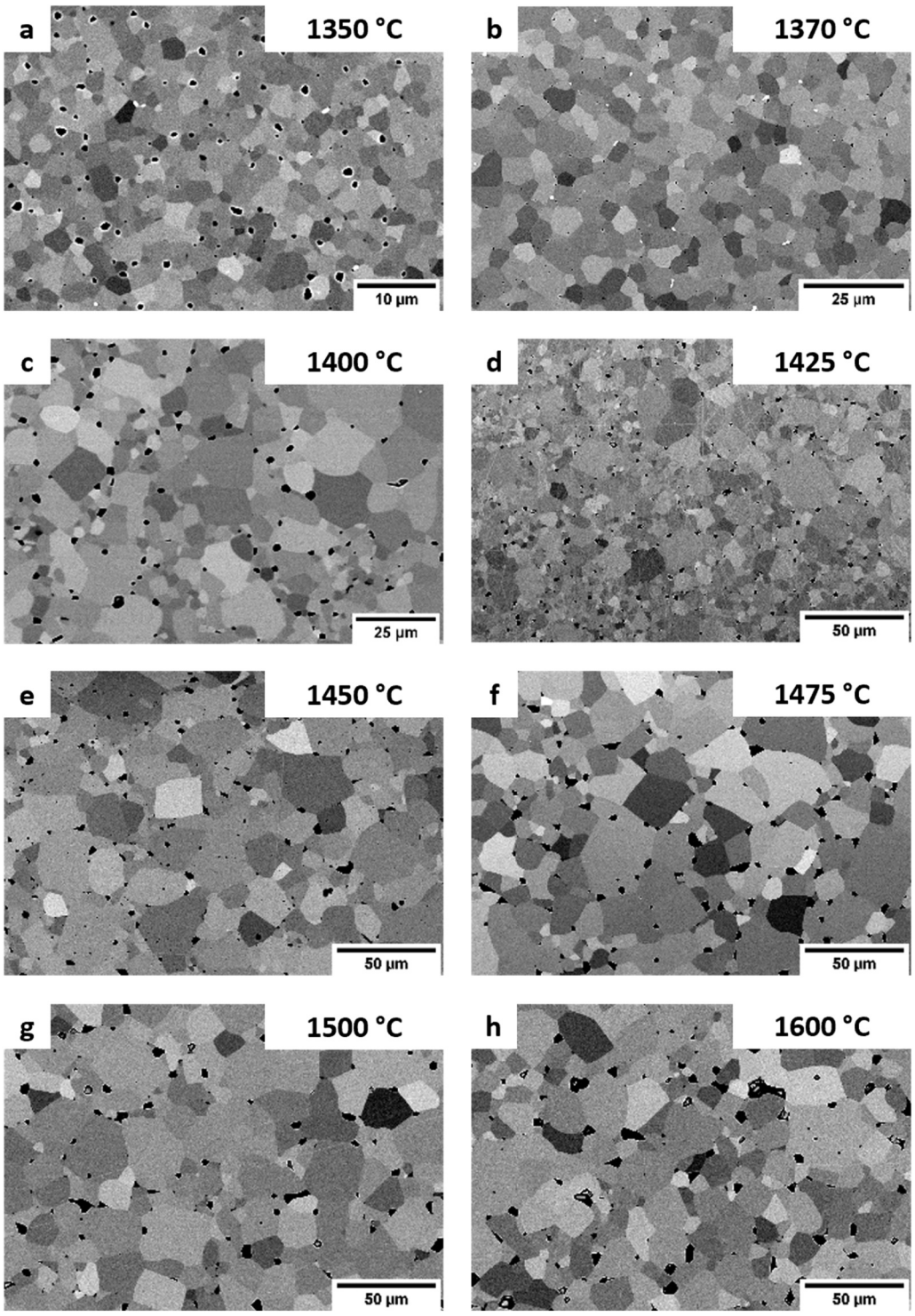


Fig. 2. BSE- SEM images of the microstructures of Nb doped $SrTiO_3$ annealed at a) 1350 °C, b) 1370 °C, c) 1400 °C, d) 1425 °C, e) 1450 °C, f) 1475 °C and g) 1500 °C for 5 h, and h) 1600 °C for 2 h. Kindly note, that the images feature different magnifications due to the large difference in microstructure.

The impedance data from Fig. 4 were used to evaluate the bulk, specific grain boundary and total conductivity of undoped and doped $SrTiO_3$ as shown in Fig. 5. The bulk conductivities of undoped and Nb/Fe codoped $SrTiO_3$ are comparable while the GB conductivity of Nb/Fe codoped $SrTiO_3$ is higher than that of the undoped sample. The total conductivity of both samples is similar. Fe doping increases bulk, GB and total conductivity compared to the undoped material. Nb doping increases the total conductivity even more than Fe doping (Fig. 5a).

3.3. Space charge characterization

Space charge layers in doped and undoped $SrTiO_3$ samples were evaluated using the impedance data from Section 3.2. Space charge layer thicknesses and potentials were determined according to the Mott-Schottky model. No space charge layer thickness and potentials could be determined for the Nb doped $SrTiO_3$ (see Section 3.2). A summary of the space charge properties of undoped, Fe doped and Nb/Fe codoped $SrTiO_3$ are given in Table 2.

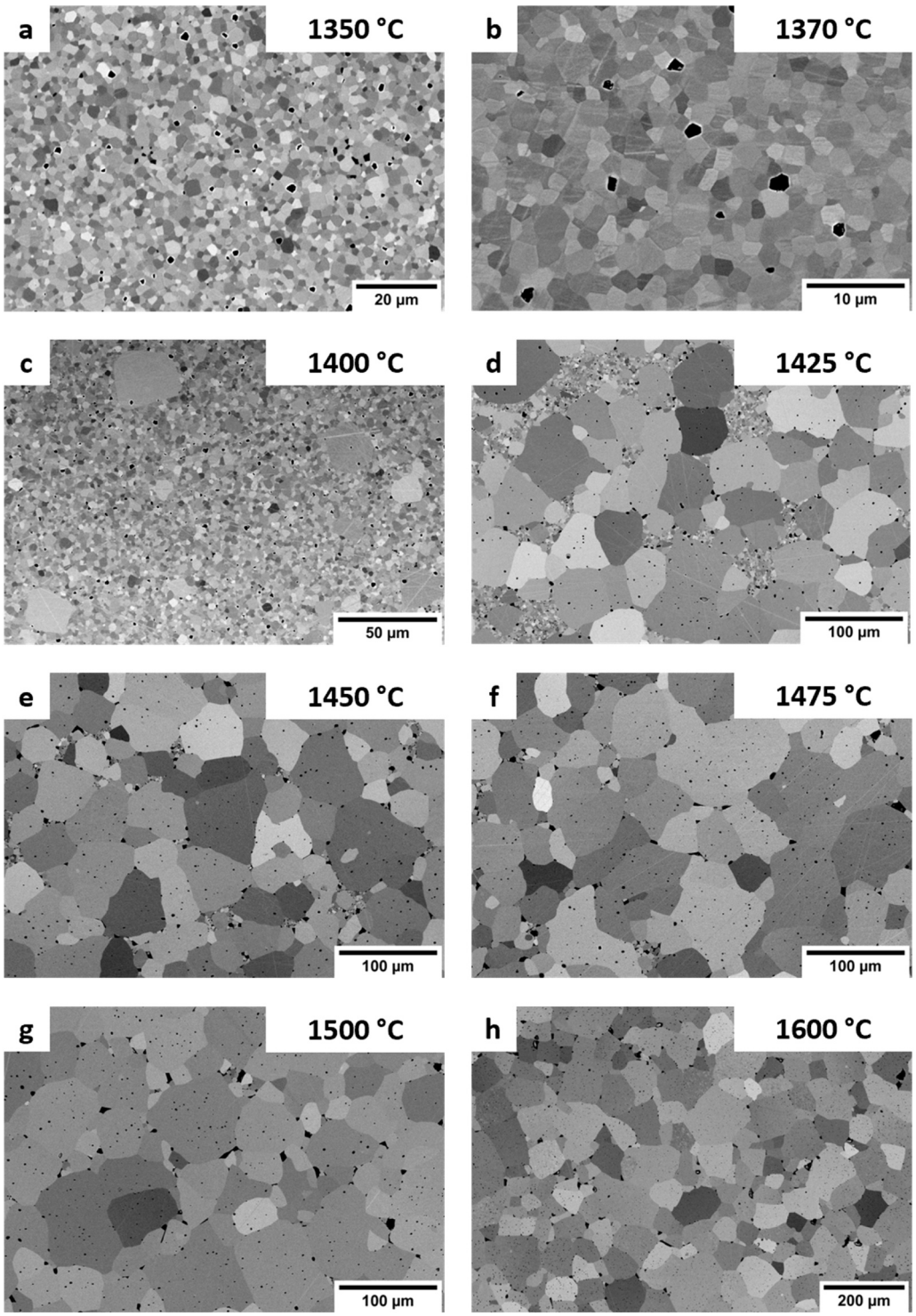


Fig. 3. BSE-SEM images of the microstructures of Nb/Fe codoped $SrTiO_3$ annealed at a) 1350 °C, b) 1370 °C, c) 1400 °C, d) 1425 °C, e) 1450 °C, f) 1475 °C and g) 1500 °C for 5 h, and h) 1600 °C for 2 h. Kindly note, that the micrographs different magnifications due to the large difference in microstructure.

According to the data from Table 2, undoped samples have the thickest space charge layers and also the highest space charge potential. The values fit the general expectations for space charge layer in undoped $SrTiO_3$ being between 5 nm and 100 nm with potential around 0.4 V. The Fe doped sample features a thinner space charge layer width (45 nm) than the undoped $SrTiO_3$ sample, yet its space charge potential is on average slightly lower (Table 2). The evaluated space charge thickness of the Nb/Fe codoped $SrTiO_3$ is also thinner than that of undoped $SrTiO_3$ but slightly thicker than that of Fe doped $SrTiO_3$. Nb/Fe codoped $SrTiO_3$ feature the lowest space charge potentials.

3.4. Grain boundary chemistry

The cationic segregation at grain boundaries in undoped and doped $SrTiO_3$ was investigated by STEM-EDS as shown in Fig. 6. Integrated line EDS line scans across the GBs in undoped, Fe-doped, Nb-doped and Nb/Fe codoped $SrTiO_3$ are shown in Fig. 7.

The grain boundary of the undoped $SrTiO_3$ shows Sr depletion and

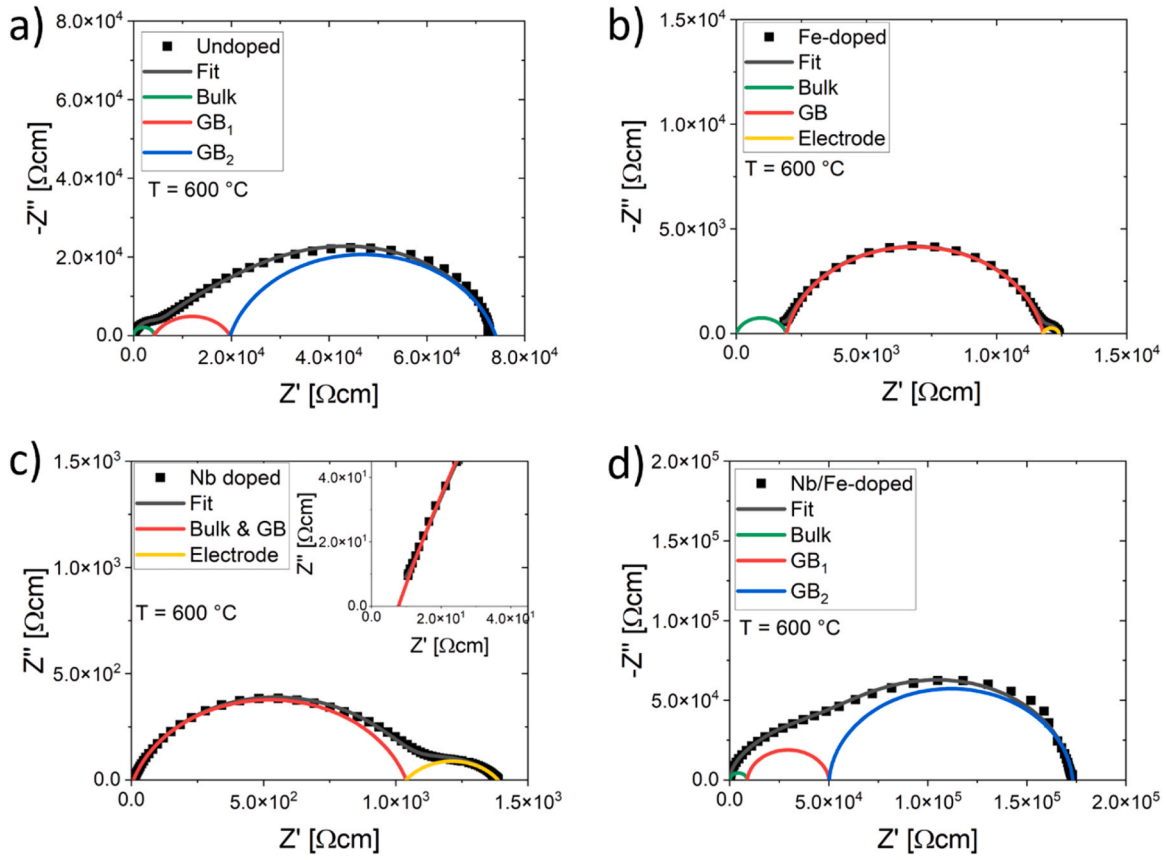


Fig. 4. Nyquist impedance Plots of the a) undoped $SrTiO_3$, b) Fe-doped $SrTiO_3$, c) Nb-doped $SrTiO_3$ and d) Nb/Fe codoped $SrTiO_3$ annealed at 1350 °C for 10 h. Note the different scale. A direct comparison of the data is shown in Fig. S4.

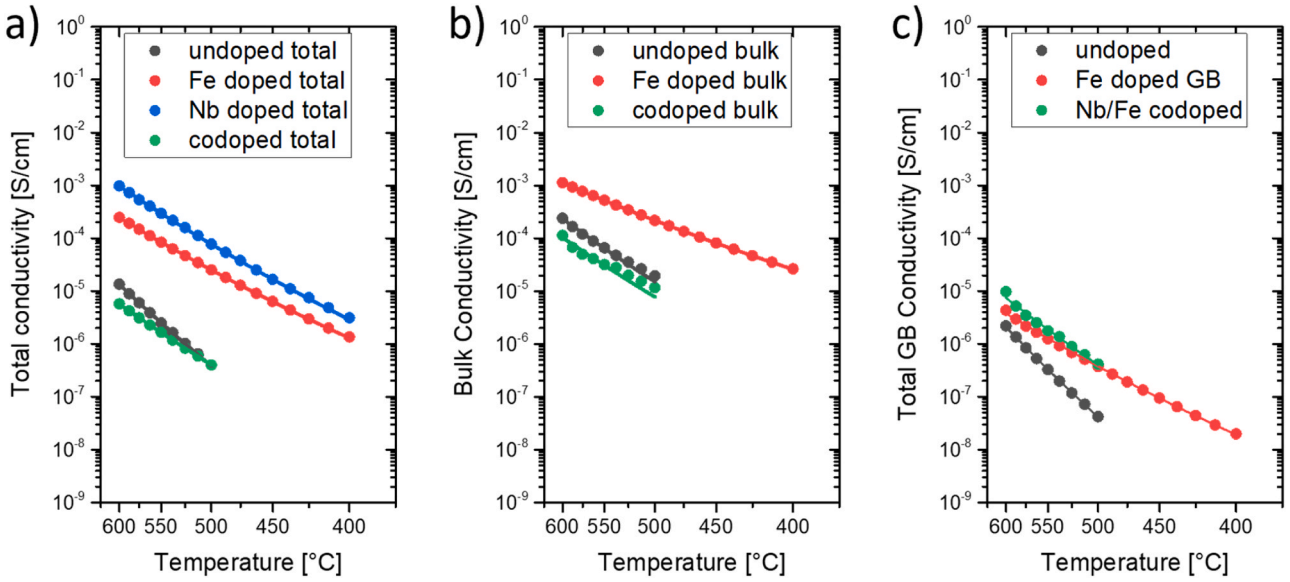


Fig. 5. The a) total, b) bulk and c) GB conductivity of undoped, Fe-doped, Nb-doped and Nb/Fe-doped $SrTiO_3$ samples in air for different measurement temperatures. The characterized samples are the same as in Fig. 4 (annealed at 1350 °C for 10 h).

slight Ti segregation at the grain boundary (Fig. 7a). Since the profiles are given as relative concentration and not absolute concentration, a decrease in the Sr signal should result in an increase of the Ti signal. The Fe-doped sample does not show any significant Ti segregation or Sr depletion at the grain boundary. Fe segregation is observed instead [19, 85].

No significant cationic segregation of any kind is observed at the grain boundaries of the Nb-doped $SrTiO_3$ (Fig. 7c). The different brightness in the EDS mappings (Fig. 6) and the different signal intensity in the EDS line scans (Fig. 7) are likely a result of channeling/orientation effects between the two adjacent grains.

In general, the segregation width of the cationic defects is narrow (<

Table 2
Space charge layer thickness and space charge potential of undoped, Fe-doped, Nb-doped and Nb/Fe codoped $SrTiO_3$.

Sample	λ_{MS} (nm)	$\Delta\Phi$ (V)	$\lambda_{MS,Avg.}$ (nm)	$\Delta\Phi_{Avg.}$ (V)
Undoped	86 and 105	0.29 and 0.43	103	0.41
Fe-doped	45	0.33	45	0.33
Nb/Fe codoped	55 and 90	0.12 and 0.32	70	0.19

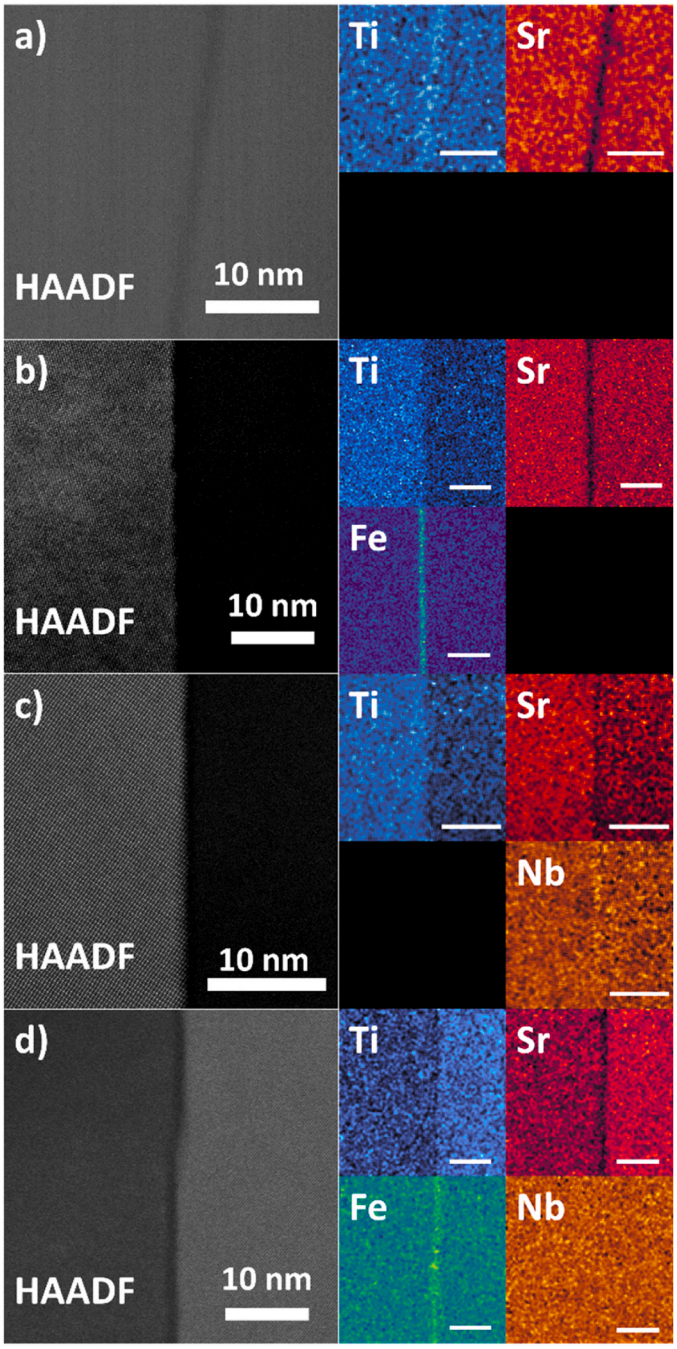


Fig. 6. STEM-EDS maps of GBs in a) undoped $SrTiO_3$, b) Fe-doped $SrTiO_3$, c) Nb-doped $SrTiO_3$ and d) Nb/Fe codoped $SrTiO_3$. Figure a) has been reprinted with permission from Elsevier [84]. All scale bars in the EDS mappings have a length of 10 nm.

10 nm). The full widths at half maximum of each segregation profile were measured to be between 1.31 nm and 4.01 nm. The segregation width is consistent with examinations of Fe doped strontium titanate at atomic resolution, showing segregation at the grain boundary which extends only 1–2 unit cells from the grain boundary core [86]. Segregation profiles are much thinner than the calculated space charge thicknesses obtained from the impedance data (Table 2). The disagreement between the two methods can be explained by the following: the cationic segregation profile represents a frozen in high temperature state (≈1000 °C) of the cations at the GB, below which cations are immobile. However, the space charge widths determined by EIS probe the space charge layer formed by high mobility defects ($V_O^{\cdot\cdot}$ or $h^{\cdot}$) that are mobile at the temperatures used during EIS analysis (< 1000 °C) [87,88].

The Gibbsian interfacial excess of each cationic species at the GBs from Fig. 6 and Fig. 7 are shown in Table 3. All samples show clear Sr depletion at their GBs of 5–10 atoms/nm^2. For context, a GB excess of −6.6 at/nm^2 would relate to a single missing plane of Sr atoms at the GB, assuming a {100} oriented GB plane. The GB excess calculation collapses all depletion/segregation onto a single plane, so does not take into account the width of segregation around the GB. The GBs of samples containing Nb also show Ti depletion the GB. Undoped and Fe doped $SrTiO_3$ show Ti segregation. GB excess calculations show slight Nb segregation at the GB region is present for Nb doped sample. The Nb/Fe doped sample does not show Nb segregation (within the error of measurement). Even though the Fe doped samples have twice the Fe content of the Nb/Fe codoped samples, the excess of Fe cations is nearly identical at the analyzed GBs.

4. Discussion

4.1. Solute drag

As mentioned before the non-Arrhenius grain growth behavior of undoped $SrTiO_3$ is believed to be caused by the coexistence of two GB types [43]: slow-migrating and fast-migrating GBs. The different migration rates were correlated to different GB chemistries and it was argued that an intrinsic drag force acts on the slow-migrating GBs. Therefore, solute drag effect are hypothesized to control grain growth in undoped and Fe-doped $SrTiO_3$ materials studied in the current work.

Evidence for this can be found in the grain growth behavior of Fe-doped and Nb/Fe codoped $SrTiO_3$. Small grains in Fe-doped or Nb/Fe doped $SrTiO_3$ have similar grain growth rates which follow the same overall trend as the slow-growing grains in undoped $SrTiO_3$ (dashed line in Fig. 1 below 1425 °C). The fact that both Fe-doped and Nb/Fe doped $SrTiO_3$ feature nearly identical Fe segregation/GB excess of Fe (Fig. 6, Fig. 7 and Table 3) and similar average grain growth rates (Fig. 1) indicate that the Fe segregation slows down the grain boundary migration rates. This correlation is consistent with to the classical solute drag model.

Nb/Fe doped samples experience abnormal grain growth above temperatures of 1400 °C. The grain growth rates of large grains in the Nb/Fe codoped $SrTiO_3$ is comparable to those of large grains in undoped $SrTiO_3$. In undoped $SrTiO_3$ small grains had on average more Ti excess at the GB while large grains were more stoichiometric [89,90]. If the grain growth in Nb/Fe doped and undoped $SrTiO_3$ are both governed by the same phenomena (solute drag), the GB composition of large grains should differ from that of small grains in Nb/Fe codoped $SrTiO_3$. Yet, no significant difference in GB chemistry between small and large grains could be identified (see Supplementary Section Figure S3). This might be explained by the small sample size of GBs analyzed in the current study and the fact that even the GB composition in undoped $SrTiO_3$ had significant standard deviation.

Pure Nb doping leads to very different grain growth behavior compared to the undoped, Fe doped and Fe/Nb codoped $SrTiO_3$ (Section 3.1). The difference might be related to a change in defect chemistry. The primary compensation mechanism in Nb-doped (donor doped)

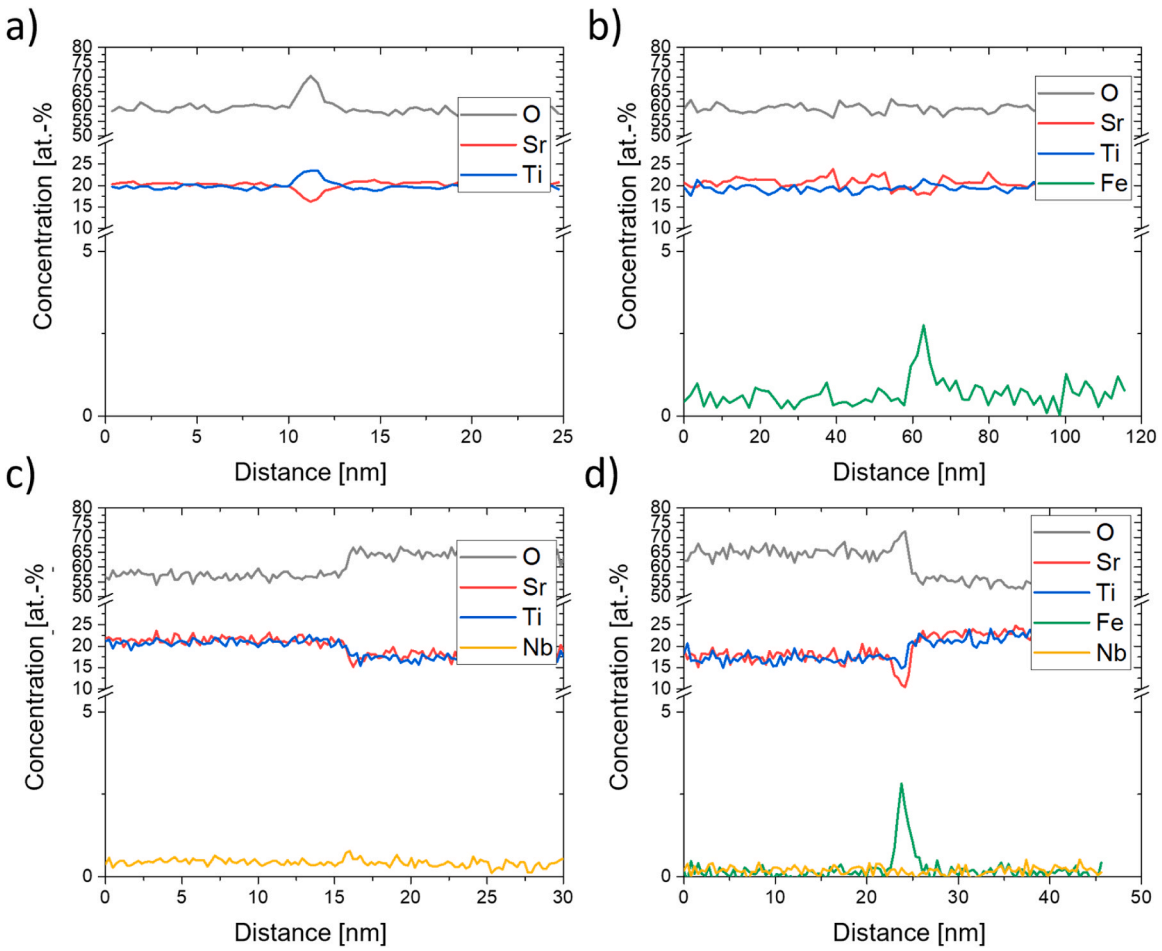


Fig. 7. Integrated EDS lines scans of a) a GB in undoped $SrTiO_3$ between two small grains, of b) a GB in Fe-doped $SrTiO_3$, of c) a GB in Nb-doped $SrTiO_3$ and of d) a GB in Nb/Fe codoped $SrTiO_3$. Figure a) has been reprinted with permission from Elsevier [84].

Table 3
Gibbsian GB excess of cationic species at the GBs in undoped, Fe doped, Nb doped and Nb/Fe codoped $SrTiO_3$ samples from Fig. 7. Detection limits for each element represent the average detection limit from measurements of each element. The full width at half maximum (FWHM) of each segregation profiles from Fig. 7 are also included.

Sample	GB Excess (atoms/nm^2)				FWHM
	Sr	Ti	Fe	Nb	(nm)
Undoped	−10.2 ± 1.3	2.6 ± 1.1	-	-	1.31 ± 0.11
Fe doped	−5.1 ± 0.5	0.7 ± 0.4	2.6 ± 0.1	-	4.01 ± 0.56
Nb doped	−10.6 ± 0.6	−5.6 ± 1.0	-	1.4 ± 0.6	-
Nb+Fe doped	−9.0 ± 2.1	−2.0 ± 1.1	2.6 ± 0.3	0.2 ± 0.3	1.35 ± 0.07
Detection Limit	0.5	0.4	0.3	0.2	

$SrTiO_3$ is the formation of V''_{Sr} instead of the formation of $V^{\cdot\cdot}_O$. The lower bulk concentration of $V^{\cdot\cdot}_O$ will alter the GB defect chemistry and by that the space charge potential at the GBs. In the case of $BaTiO_3$, negative grain boundary core charges for donor doped materials were reported [91] which would completely change grain boundary segregation and migration. A reduction in space charge potential and change in GB chemistry due to donor doping fits previous observations for Nb doped $SrTiO_3$ where little Nb segregation was observed [85,92] and bulk impedance was hard to distinguish from GB impedance [81,82]. Accordingly, an impact on GB migration cannot be ruled out. Nb doped $SrTiO_3$ seems to experience grain growth stagnation for certain annealing conditions (Table S2). Grain growth stagnation can have multiple causes: solute drag, pore drag, Zener pinning, critical driving forces for grain growth which have to be overcome, e.g. from nucleation barriers [93] or disconnection motion [94–97]. Since Nb-doped $SrTiO_3$ has a comparably large porosity (4 %), pore drag might be a reasonable explanation. This is also relevant since densification and grain growth are most-likely happening at the same time in these samples (Nb-doped samples have not been pre-sintered). Another explanation is Nb segregation leading to solute drag based on the GB composition shown in Table 3. Yet, it is not possible to designate the mechanism causing grain growth stagnation based on the data presented in this study.

In general, solute drag seems to govern grain growth behavior of $SrTiO_3$. This is indicated by Fig. 8 where the grain growth rate decreases with increasing dopant excess at GBs. The result is comparable to observations of previous studies where the grain growth rate of Fe doped $SrTiO_3$ decreased with increasing Fe segregation [19]. Note that the GB excess is microscopic, local data (Fig. 8) while the grain growth coefficients are averaged, macroscopic data. Fig. 8 is therefore a simplification and a comparison might not be justifiable.

4.2. *Electric bulk properties of undoped and doped $SrTiO_3$*

To understand the electric properties of bulk $SrTiO_3$, the defect chemistry has to be understood. The conductivity is proportional to the number of charge carriers and their mobility through the material. An increase in defect concentration in $SrTiO_3$ ceramics should thereby

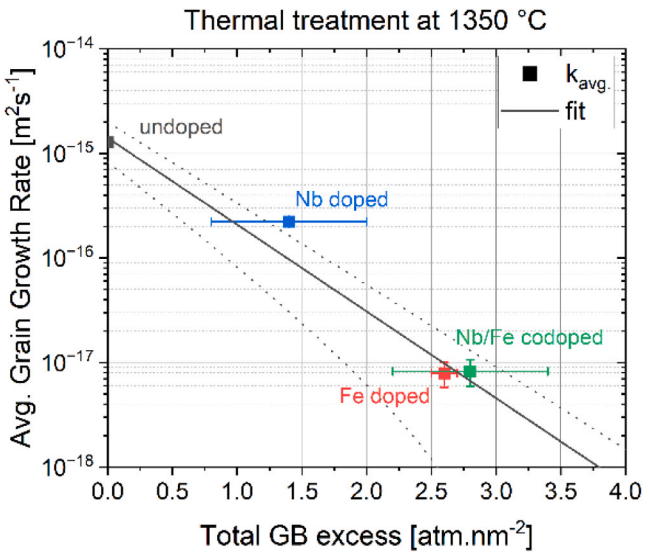


Fig. 8. Grain growth rate of differently doped $SrTiO_3$ depending on the combined GB excess of Fe and Nb segregation. A fitting curve (grey) with its range of uncertainty (dotted, grey) has been added to the figure.

increase the bulk conductivity.

Undoped $SrTiO_3$ is usually slightly acceptor doped due to natural impurities which act as acceptors [3,4]. Acceptor doping (A'_{Ti}) introduces additional oxygen vacancies to compensate the negative charge (see Eq. 10). In oxidizing conditions, $V_O^{\cdot\cdot}$ are filled by oxygen ions from the atmosphere introducing electron holes $h^{\cdot}$ into near-valence band states (see Eq. 11). If enough $V_O^{\cdot\cdot}$ are filled, $SrTiO_3$ becomes a p-type semiconductor which is the case for undoped and slightly acceptor doped $SrTiO_3$ (in air between 400 °C and 600 °C) [58]. For that reason, it is to be expected that both the undoped samples and Fe doped samples are p-type semiconductors (Eq. 12).

$$A_2O_3 \rightarrow 2A'_{Ti} + 3O_O^x + V_O^{\cdot\cdot} \quad (10)$$

$$V_O^{\cdot\cdot} + \frac{1}{2}O_2 \rightarrow O_O^x + 2h^{\cdot} \quad (11)$$

$$A_2O_3 + \frac{1}{2}O_2 \rightarrow 2A'_{Ti} + 4O_O^x + 2h^{\cdot} \quad (12)$$

Since Fe doping introduces additional defects such as $V_O^{\cdot\cdot}$ or $h^{\cdot}$, an increase in bulk conductivity compared to the undoped material is expected for Fe doped $SrTiO_3$. This can be observed in Fig. 5b, where the bulk conductivity of Fe-doped $SrTiO_3$ is about one order of magnitude higher than that of undoped $SrTiO_3$.

In the case of donor (D) and acceptor (A) codoping, the donor and acceptor dopants are charge-compensating each other. If they are present at the same concentration, they should not introduce any other charged defects such as $V_O^{\cdot\cdot}$, $h^{\cdot}$, electrons e' or strontium vacancies V''_{Sr}. This is expressed by Eq. 13.

$$A_2O_3 + D_2O_5 \rightarrow 2A'_{Ti} + 2D_{Ti}^{\cdot} + 8O_O^x \quad (13)$$

Accordingly, undoped and donor acceptor codoped $SrTiO_3$ should have similar mobile charge carrier activities ($[V_O^{\cdot\cdot}]$, p) and by that similar bulk conductivities. This can indeed be observed in Fig. 5b where the bulk conductivity of undoped and Nb/Fe codoped $SrTiO_3$ are nearly identical.

Purely donor doped $SrTiO_3$ features an entirely different defect chemistry than the other samples of this study. Donors have a positive charge that is compensated by e' (Eq. 14).

$$D_2O_5 \rightarrow 2D_{Ti}^{\cdot} + 4O_O^x + \frac{1}{2}O_2\uparrow + 2e' \quad (14)$$

Under Oxidizing conditions (Eq. 15) V''_{Sr} are preferentially formed in $SrTiO_3$ instead of e'.

$$\frac{1}{2}O_2(g) \rightarrow \quad O_O^x + V''_{Sr} + 2h^{\cdot} \quad (15)$$

Combining Eq. 14 and Eq. 15 it becomes obvious that the primary charge compensation mechanism in donor doped $SrTiO_3$ under oxidizing conditions are also V''_{Sr} (Eq. 16) [3].

$$D_2O_5 \rightarrow 2D_{Ti}^{\cdot} + 5O_O^x + V''_{Sr} \quad (16)$$

Accordingly, the charge carrier concentration and the bulk conductivity should decrease with increasing oxygen partial pressure. Based on literature, a slight increase in bulk conductivity compared to undoped $SrTiO_3$ is expected for a given oxygen partial pressure [3]. The bulk and GB impedance could not be identified in the impedance data (see Fig. 4c); a separate evaluation of the bulk and GB conductivity was not possible. The difficulty in distinguishing GB and bulk impedance for Nb-doped $SrTiO_3$ annealed in oxidizing conditions is known from literature [81,82]. Still, an increase in total conductivity of Nb-doped $SrTiO_3$ compared to undoped $SrTiO_3$ can be observed (Fig. 5a). Whether this increase can be attributed to an increase in bulk conductivity, GB conductivity or both cannot be determined using the impedance data presented in this study.

4.3. Changes in space charge layer composition and properties by doping

The GB impedance of undoped and Nb/Fe codoped $SrTiO_3$ was fitted with two RQ-circuits to attribute for the GB impedance arc distortion. In a previous publication, the presence of a distorted GB impedance arc that was fitted with two RQ-circuits was correlated to a large variety in GB conductivity distribution [46]. This complicates the comparison with samples whose impedance plots did not feature a distorted GB impedance arc. For that reason, the average or total GB resistance, capacitance and relaxation time were used when evaluating electric GB properties.

Doping a ceramic should not only influence the bulk properties of a material but also its GB properties. This could be seen in Section 4.1 where changes in GB composition were correlated to different grain growth kinetics. Based on the space charge layer model a different GB chemistry should also alter the space charge layer and the GB conductivity.

The GB conductivities of Fe doped and Nb/Fe codoped $SrTiO_3$ are higher than that of undoped $SrTiO_3$ (Fig. 5c). The increase in GB conductivity is probably related to the GB chemistry because Fe segregates at the GB of Fe doped and Nb/Fe doped $SrTiO_3$ (Fig. 6 and Fig. 7) and both have a higher GB conductivity. It is suspected that the low GB conductivity of undoped $SrTiO_3$ is caused by a space charge layer resulting from a positive GB core charge which is compensated by defects accumulating at the GB. A correlation between $\Delta\Phi$ and GB conductivity has been previously observed for undoped $SrTiO_3$ [46]. In the current manuscript, a correlation between GB chemistry, conductivity and $\Delta\Phi$ is indeed observed since samples with Fe segregation at their GB have higher GB conductivities and lower space charge potentials than undoped $SrTiO_3$. Yet, a clear correlation between GB chemistry and electric properties is not observed. Fe doped and Nb/Fe $SrTiO_3$ might have similar GB conductivity yet different space charge potentials. A possible explanation might be the GB defect chemistry of Fe-doped and Nb/Fe codoped samples, which have to be compared with caution. This is due to the low number of GBs characterized by STEM-EDS, and the fact that only the cationic segregation behavior could be analyzed. Accordingly, the concentration of electrons, electron holes or anionic defects at the GBs is unknown. Also, the total charge carrier concentration in a material should contribute to the conductivity of the GB.

No information on the electric properties of the GBs of Nb doped $SrTiO_3$ could be obtained in the current study which was already expected due to low GB segregation in these samples (see Section 4.1) [81,

82].

5. Summary and conclusion

In the current study, the correlation between grain boundary composition and electrical properties as well as grain growth behavior of Nb-doped and Nb/Fe-doped $SrTiO_3$ was investigated. Data were compared to previous studies on undoped and Fe-doped $SrTiO_3$. Electrochemical impedance spectroscopy was utilized for electrical characterization. Space charge properties were evaluated based on the Mott-Schottky model and compared with cationic segregation profiles obtained from STEM-EDS characterization. Grain growth studies for Nb-doped and Nb/Fe codoped material were performed and correlated to the cationic segregation profiles. All results were discussed in the frame work of defect chemistry, solute drag and space charge.

The experimental results indicate that solute drag effects dominate the grain growth behavior of $SrTiO_3$. Significant dopant segregation was observed by STEM-EDS characterization which correlates to changes in grain growth behavior. Slowed grain growth kinetics leading to submicron grain sizes in combination with strong Fe segregation at GB are an indication for solute drag in Fe doped $SrTiO_3$. Grain growth stagnation in Nb doped $SrTiO_3$ also supports the argument for solute drag, yet the relatively high porosity of Nb doped $SrTiO_3$ might also explain the grain growth stagnation. Codoping of $SrTiO_3$ with acceptor (Fe) and donor (Nb) leads to significant abnormal grain growth, where the small grain growth population had the grain growth kinetics of Fe doped $SrTiO_3$ and the large grains had the grain growth kinetics of large grains in undoped $SrTiO_3$. The grain growth rate of $SrTiO_3$ ceramics decreased with an increase in Gibbsian GB excess of dopant cations which fit previous observation experimental in Fe doped $SrTiO_3$.

The segregation of Fe and other defects (V''_{Sr}, V'^{4}_{Ti} or Nb) was correlated to the decrease in space charge potential in Fe doped and Nb/Fe codoped $SrTiO_3$. Both materials have similar GB conductivities σ_{GB} and a similar excess of Fe cations at their GB. Yet even though Fe segregation leads to similar σ_{GB}, the space charge potentials deviate from one another. A final conclusion on the cause could not be found because of the limited knowledge on the GB chemistry (n, p and $[V_O^{\cdot\cdot}]$).

Dopants are often used to improve the electrical properties of functional ceramics in energy applications but tend to segregate at grain boundaries influencing microstructural evolution by solute drag in many ceramic materials, such as $BaTiO_3$ or ZrO_2. The current study demonstrates the importance of understanding the influence of dopants on the grain growth behavior and electrical properties, which are interconnected. Accordingly, the observed effects can be used to tailor microstructures and conductivities which are detrimental to the application of energy materials.

CRediT authorship contribution statement

Wolfgang Rheinheimer: Writing – review & editing, Validation, Supervision, Software, Resources, Project administration, Funding acquisition, Conceptualization. **Dylan Jennings:** Writing – review & editing, Validation, Methodology, Investigation, Formal analysis, Data curation. **Zahler Marc Pascal:** Writing – review & editing, Writing – original draft, Visualization, Methodology, Investigation, Formal analysis, Data curation, Conceptualization. **Olivier Guillon:** Writing – review & editing, Validation, Software, Resources.

Declaration of Competing Interest

The authors declare that they have no known competing financial interests or personal relationships that could have appeared to influence the work reported in this paper.

Acknowledgements

The authors acknowledge funding by the DFG via the Emmy Noether Programme (Rh 146/1–1) and the CRC 1548 FLAIR (B04). The authors thank Hitachi High-Technologies for providing access to the HF5000 STEM which was used for this work.

Appendix A. Supporting information

Supplementary data associated with this article can be found in the online version at doi:10.1016/j.jeurceramsoc.2025.117965.

References

[1] D.M. Smyth, The defect chemistry of metal oxides, Oxford University Press, New York, 2000.
[2] J. Nowotny, T. Bak, E.C. Dickey, W. Sigmund, M.A. Alim, Electrical conductivity, thermoelectric power, and equilibration kinetics of Nb-doped TiO_2, J. Phys. Chem. A 120 (2016) 6822–6837, https://doi.org/10.1021/acs.jpca.6b04104.
[3] R. Moos, K.H. Haerdtl, Defect chemistry of donor-doped and undoped strontium titanate ceramics between 1000° and 1400°C, J. Am. Ceram. Soc. 80 (2005) 2549–2562, https://doi.org/10.1111/j.1151-2916.1997.tb03157.x.
[4] R.A.D. Souza, J. Fleig, R. Merkle, J. Maier, $SrTiO_3$: a model electroceramic, IJMR 94 (2003) 218–225, https://doi.org/10.3139/ijmr-2003-0043.
[5] G. Liu, J. Wolfman, C. Autret-Lambert, J. Sakai, S. Roger, M. Gervais, F. Gervais, Microstructural and dielectric properties of Ba0.6Sr0.4Ti1−xZrxO3 based combinatorial thin film capacitors library, J. Appl. Phys. 108 (2010) 114108, https://doi.org/10.1063/1.3514153.
[6] H. Yokokawa, N. Sakai, T. Horita, K. Yamaji, M.E. Brito, Electrolytes for solid-oxide fuel cells, MRS Bull. 30 (2005) 591–595, https://doi.org/10.1557/mrs2005.166.
[7] X. Yao, B. Huang, J. Yin, G. Peng, Z. Huang, C. Gao, D. Liu, X. Xu, All-solid-state lithium batteries with inorganic solid electrolytes: review of fundamental science, Chin. Phys. B 25 (2016) 018802, https://doi.org/10.1088/1674-1056/25/1/018802.
[8] F. Tietz, Materials selection for solid oxide fuel cells, MSF 426–432 (2003) 4465–4470, https://doi.org/10.4028/www.scientific.net/MSF.426-432.4465.
[9] G. Gregori, R. Merkle, J. Maier, Ion conduction and redistribution at grain boundaries in oxide systems, Prog. Mater. Sci. 89 (2017) 252–305, https://doi.org/10.1016/j.pmatsci.2017.04.009.
[10] R. Waser, R. Hagenbeck, Grain boundaries in dielectric and mixed-conducting ceramics, Acta Mater. 48 (2000) 797–825, https://doi.org/10.1016/S1359-6454(99)00367-5.
[11] X. Guo, J. Fleig, J. Maier, Separation of Electronic and Ionic Contributions to the Grain Boundary Conductivity in Acceptor-Doped $SrTiO_3$, J. Electrochem. Soc. 148 (2001) J50, https://doi.org/10.1149/1.1389344.
[12] D.S. Mebane, R.A. De Souza, A generalised space-charge theory for extended defects in oxygen-ion conducting electrolytes: from dilute to concentrated solid solutions, Energy Environ. Sci. 8 (2015) 2935–2940, https://doi.org/10.1039/C5EE02060C.
[13] R.A. De Souza, The formation of equilibrium space-charge zones at grain boundaries in the perovskite oxide $SrTiO_3$, Phys. Chem. Chem. Phys. 11 (2009) 9939, https://doi.org/10.1039/b904100a.
[14] R.A. De Souza, E.C. Dickey, The effect of space-charge formation on the grain-boundary energy of an ionic solid, Philos. Trans. R. Soc. A. 377 (2019) 20180430, https://doi.org/10.1098/rsta.2018.0430.
[15] W. Rheinheimer, J.P. Parras, J. Preusker, R.A. De Souza, M.J. Hoffmann, Grain growth in strontium titanate in electric fields: The impact of space-charge on the grain-boundary mobility, J. Am. Ceram. Soc. 102 (2019) 3779–3790, https://doi.org/10.1111/jace.16217.
[16] P. Debye, E. Hückel, Zur Theorie der Elektrolyte. I. Gefrierpunktserniedrigung und verwandte Erscheinungen, Phys. Z. 24 (1923) 305.
[17] S.-J.L. Kang, S.-Y. Ko, S.-Y. Moon, Mixed control of boundary migration and the principle of microstructural evolution, J. Ceram. Soc. Jpn. 124 (2016) 259–267, https://doi.org/10.2109/jcersj2.15262.
[18] M.N. Rahaman, R. Manalert, Grain boundary mobility of $BaTiO_3$ doped with aliovalent cations, J. Eur. Ceram. Soc. 18 (1998) 1063–1071, https://doi.org/10.1016/S0955-2219(97)00215-X.
[19] M.P. Zahler, S.M. Kraschewski, H. Störmer, D. Gerthsen, M. Bäurer, W. Rheinheimer, Grain growth and segregation in Fe-doped $SrTiO_3$: experimental evidence for solute drag, J. Eur. Ceram. Soc. (2022) S095522192200961X, https://doi.org/10.1016/j.jeurceramsoc.2022.11.074.
[20] R. Moshe, W.D. Kaplan, The combined influence of Mg and Ca on microstructural evolution of alumina, J. Am. Ceram. Soc. 102 (2019) 4882–4887, https://doi.org/10.1111/jace.16321.
[21] S.J. Dillon, M. Tang, W.C. Carter, M.P. Harmer, Complexion: a new concept for kinetic engineering in materials science, Acta Mater. 55 (2007) 6208–6218, https://doi.org/10.1016/j.actamat.2007.07.029.
[22] J. Fleig, The grain boundary impedance of random microstructures: numerical simulations and implications for the analysis of experimental data, Solid State Ion. 150 (2002) 181–193, https://doi.org/10.1016/S0167-2738(02)00274-6.
[23] J.W. Cahn, The impurity-drag effect in grain boundary motion, Acta Metall. 10 (1962) 789–798, https://doi.org/10.1016/0001-6160(62)90092-5.

[24] M. Hillert, Solute drag, solute trapping and diffusional dissipation of Gibbs energy, Acta Mater. 47 (1999) 4481–4505, https://doi.org/10.1016/S1359-6454(99)00336-5.

[25] J.D. Powers, A.M. Glaeser, Grain boundary migration in ceramics, Interface Sci. 6 (1998) 23–39, https://doi.org/10.1023/A:1008656302007.

[26] K.S.N. Vikrant, W. Rheinheimer, R.E. García, Electrochemical drag effect on grain boundary motion in ionic ceramics, Npj Comput. Mater. 6 (2020) 165, https://doi.org/10.1038/s41524-020-00418-z.

[27] P.-L. Chen, I.-W. Chen, Grain Growth in CeO_2: Dopant Effects, Defect Mechanism, and Solute Drag, J. Am. Ceram. Soc. 79 (1996) 1793–1800, https://doi.org/10.1111/j.1151-2916.1996.tb07997.x.

[28] K.S.N. Vikrant, W. Rheinheimer, H. Sternlicht, M. Bäurer, R.E. García, Electrochemically-driven abnormal grain growth in ionic ceramics, Acta Mater. 200 (2020) 727–734, https://doi.org/10.1016/j.actamat.2020.08.027.

[29] M. Kindelmann, K. Ran, W. Rheinheimer, K. Morita, J. Mayer, M. Bram, O. Guillon, Segregation-controlled densification and grain growth in rare earth-doped Y_2O_3, J. Am. Ceram. Soc. 104 (2021) 4946–4959, https://doi.org/10.1111/jace.17907.

[30] S.G. Kim, Y.B. Park, Grain boundary segregation, solute drag and abnormal grain growth, Acta Mater. 56 (2008) 3739–3753, https://doi.org/10.1016/j.actamat.2008.04.007.

[31] S.-Y. Choi, D.-Y. Yoon, S.-J.L. Kang, Kinetic formation and thickening of intergranular amorphous films at grain boundaries in barium titanate, Acta Mater. 52 (2004) 3721–3726, https://doi.org/10.1016/j.actamat.2004.04.026.

[32] J.G. Fisher, S.-J.L. Kang, Microstructural changes in $(K_{0.5}Na_{0.5})NbO_3$ ceramics sintered in various atmospheres, J. Eur. Ceram. Soc. 29 (2009) 2581–2588, https://doi.org/10.1016/j.jeurceramsoc.2009.02.006.

[33] M.N. Kelly, W. Rheinheimer, M.J. Hoffmann, G.S. Rohrer, Anti-thermal grain growth in $SrTiO_3$: Coupled reduction of the grain boundary energy and grain growth rate constant, Acta Mater. 149 (2018) 11–18, https://doi.org/10.1016/j.actamat.2018.02.030.

[34] G.S. Rohrer, Grain boundary energy anisotropy: a review, J. Mater. Sci. 46 (2011) 5881–5895, https://doi.org/10.1007/s10853-011-5677-3.

[35] G.S. Rohrer, INFLUENCE OF INTERFACE ANISOTROPY ON GRAIN GROWTH AND COARSENING, Annu. Rev. Mater. Res. 35 (2005) 99–126, https://doi.org/10.1146/annurev.matsci.33.041002.094657.

[36] W. Rheinheimer, M. Bäurer, C.A. Handwerker, J.E. Blendell, M.J. Hoffmann, Growth of single crystalline seeds into polycrystalline strontium titanate: Anisotropy of the mobility, intrinsic drag effects and kinetic shape of grain boundaries, Acta Mater. 95 (2015) 111–123, https://doi.org/10.1016/j.actamat.2015.05.019.

[37] A. Subramaniam, C.T. Koch, R.M. Cannon, M. Rühle, Intergranular glassy films: An overview, Materials Science Engineering A 422 (2006) 3–18, https://doi.org/10.1016/j.msea.2006.01.004.

[38] P.R. Cantwell, M. Tang, S.J. Dillon, J. Luo, G.S. Rohrer, M.P. Harmer, Grain boundary complexions, Acta Mater. 62 (2014) 1–48, https://doi.org/10.1016/j.actamat.2013.07.037.

[39] J.W. Cahn, Critical point wetting, J. Chem. Phys. 66 (1977) 3667–3672, https://doi.org/10.1063/1.434402.

[40] W. Rheinheimer, M.J. Hoffmann, Grain growth transitions of perovskite ceramics and their relationship to abnormal grain growth and bimodal microstructures, J. Mater. Sci. 51 (2016) 1756–1765, https://doi.org/10.1007/s10853-015-9535-6.

[41] B.-K. Lee, S.-Y. Chung, S.-J.L. Kang, Grain boundary faceting and abnormal grain growth in BaTiO3, Acta Mater. 48 (2000) 1575–1580, https://doi.org/10.1016/S1359-6454(99)00434-6.

[42] G. Han, J. Ryu, C. Ahn, W. Yoon, J. Choi, B. Hahn, J. Kim, J. Choi, D. Park, High Piezoelectric Properties of KNN -Based Thick Films with Abnormal Grain Growth, J. Am. Ceram. Soc. 95 (2012) 1489–1492, https://doi.org/10.1111/j.1551-2916.2012.05139.x.

[43] W. Rheinheimer, E. Schoof, M. Selzer, B. Nestler, M.J. Hoffmann, Non-Arrhenius grain growth in strontium titanate: Quantification of bimodal grain growth, Acta Mater. 174 (2019) 105–115, https://doi.org/10.1016/j.actamat.2019.05.040.

[44] W. Rheinheimer, M.J. Hoffmann, Non-Arrhenius behavior of grain growth in strontium titanate: New evidence for a structural transition of grain boundaries, Scr. Mater. 101 (2015) 68–71, https://doi.org/10.1016/j.scriptamat.2015.01.021.

[45] W. Rheinheimer, M.J. Hoffmann, Grain growth in perovskites: What is the impact of boundary transitions? Curr. Opin. Solid State Mater. Sci. 20 (2016) 286–298, https://doi.org/10.1016/j.cossms.2016.04.004.

[46] M.P. Zahler, D. Jennings, O. Guillon, W. Rheinheimer, Non-Arrhenius grain growth in SrTiO3: Impact on grain boundary conductivity and segregation, Acta Mater. 283 (2025) 120560, https://doi.org/10.1016/j.actamat.2024.120560.

[47] D.M. Smyth, Electrical Conductivity in Ceramics: A Review, in: J.A. Pask, A. G. Evans (Eds.), Ceramic Microstructures '86, Springer US, Boston, MA, 1987, pp. 643–655, https://doi.org/10.1007/978-1-4613-1933-7_65.

[48] F. Noll, SrTiO3 as a prototype of a mixed conductor Conductivities, oxygen diffusion and boundary effects, Solid State Ion. 86–88 (1996) 711–717, https://doi.org/10.1016/0167-2738(96)00155-5.

[49] M. Fleischer, H. Meixner, C. Tragut, Hole Mobility in Acceptor-Doped, Monocrystalline $SrTiO_3$, J. Am. Ceram. Soc. 75 (1992) 1666–1668, https://doi.org/10.1111/j.1151-2916.1992.tb04242.x.

[50] R.A. Maier, C.A. Randall, Low-Temperature Ionic Conductivity of an Acceptor-Doped Perovskite: I. Impedance of Single-Crystal $SrTiO_3$, J. Am. Ceram. Soc. 99 (2016) 3350–3359, https://doi.org/10.1111/jace.14348.

[51] I. Denk, W. Münch, J. Maier, Partial Conductivities in $SrTiO_3$: Bulk Polarization Experiments, Oxygen Concentration Cell Measurements, and Defect-Chemical Modeling, J. Am. Ceram. Soc. 78 (1995) 3265–3272, https://doi.org/10.1111/j.1151-2916.1995.tb07963.x.

[52] T. Van Dijk, A.J. Burggraaf, Grain boundary effects on ionic conductivity in ceramic $Gd_xZr_{1-x}O_{2-(x/2)}$ solid solutions, Phys. Stat. Sol. (a) 63 (1981) 229–240, https://doi.org/10.1002/pssa.2210630131.

[53] M. Leonhardt, In Situ Monitoring and Quantitative Analysis of Oxygen Diffusion Through Schottky-Barriers in SrTiO[sub 3] Bicrystals, Electrochem. SolidState Lett. 2 (1999) 333, https://doi.org/10.1149/1.1390827.

[54] R. Hagenbeck, R. Waser, Influence of temperature and interface charge on the grain-boundary conductivity in acceptor-doped $SrTiO_3$ ceramics, J. Appl. Phys. 83 (1998) 2083–2092, https://doi.org/10.1063/1.366941.

[55] A. Tschope, S. Kilassonia, R. Birringer, The grain boundary effect in heavily doped cerium oxide, Solid State Ion. 173 (2004) 57–61, https://doi.org/10.1016/j.ssi.2004.07.052.

[56] S.M. Haile, D.L. West, J. Campbell, The role of microstructure and processing on the proton conducting properties of gadolinium-doped barium cerate, J. Mater. Res. 13 (1998) 1576–1595, https://doi.org/10.1557/JMR.1998.0219.

[57] P.-L. Chen, I.-W. Chen, Grain Boundary Mobility in Y_2O_3: Defect Mechanism and Dopant Effects, J. Am. Ceram. Soc. 79 (1996) 1801–1809, https://doi.org/10.1111/j.1151-2916.1996.tb07998.x.

[58] A. Rothschild, W. Menesklou, H.L. Tuller, E. Ivers-Tiffée, Electronic Structure, Defect Chemistry, and Transport Properties of $SrTi_{1-x}Fe_xO_{3-y}$ Solid Solutions, Chem. Mater. 18 (2006) 3651–3659, https://doi.org/10.1021/cm052803x.

[59] Y.-M. Chiang, T. Takagi, Grain-Boundary Chemistry of Barium Titanate and Strontium Titanate: I, High-Temperature Equilibrium Space Charge, J. Am. Ceram. Soc. 73 (1990) 3278–3285, https://doi.org/10.1111/j.1151-2916.1990.tb06450.x.

[60] T. Shi, Y. Chen, X. Guo, Defect chemistry of alkaline earth metal (Sr/Ba) titanates, Prog. Mater. Sci. 80 (2016) 77–132, https://doi.org/10.1016/j.pmatsci.2015.10.002.

[61] R. Meyer, R. Waser, J. Helmbold, G. Borchardt, Cationic Surface Segregation in Donor-Doped $SrTiO_3$ Under Oxidizing Conditions, J. Electroceram. 9 (2002) 101–110, https://doi.org/10.1023/A:1022898104375.

[62] Y.Q. Wang, Y. Liu, M.X. Zhang, F.F. Min, Electronic, magnetic and optical properties of charge-compensated (Nb, TM = Fe, Cr)-codoped $SrTiO_3$ from first principles, Ferroelectrics 537 (2018) 68–78, https://doi.org/10.1080/00150193.2018.1528958.

[63] T. Yokoyama, Y. Iwazaki, Y. Onda, Y. Sasajima, T. Nishihara, M. Ueda, Highly piezoelectric co-doped AlN thin films for wideband FBAR applications, in: 2014 IEEE International Ultrasonics Symposium, IEEE, Chicago, IL, USA, 2014, pp. 281–288, https://doi.org/10.1109/ULTSYM.2014.0070.

[64] M. Sun, H. Liu, Z. Sun, W. Li, Donor-acceptor codoping effects on tuned visible light response of TiO2, J. Environ. Chem. Eng. 8 (2020) 104168, https://doi.org/10.1016/j.jece.2020.104168.

[65] J.E. Burke, D. Turnbull, Recrystallization and grain growth, Prog. Met. Phys. 3 (1952) 220–292, https://doi.org/10.1016/0502-8205(52)90009-9.

[66] F. De La Peña, E. Prestat, V.T. Fauske, P. Burdet, J. Lähnemann, P. Jokubauskas, T. Furnival, M. Nord, T. Ostasevicius, K.E. MacArthur, D.N. Johnstone, M. Sarahan, J. Taillon, T. Aarholt, Pquinn-Dls, V. Migunov, A. Eljarrat, J. Caron, C. Francis, T. Nemoto, T. Poon, S. Mazzucco, Actions-User, N. Tappy, N. Cautaerts, Suhas Somnath, T. Slater, M. Walls, F. Winkler, H.W. Ånes, hyperspy/hyperspy: Release v1.7.3, (2022). https://doi.org/10.5281/ZENODO.592838.

[67] K. Syed, M. Xu, K.K. Ohtaki, D. Kok, K.K. Karandikar, O.A. Graeve, W.J. Bowman, M.L. Mecartney, Correlations of grain boundary segregation to sintering techniques in a three-phase ceramic, Materialia 14 (2020) 100890, https://doi.org/10.1016/j.mtla.2020.100890.

[68] H. Sternlicht, S.A. Bojarski, G.S. Rohrer, W.D. Kaplan, Quantitative differences in the Y grain boundary excess at boundaries delimiting large and small grains in Y doped Al2O3, J. Eur. Ceram. Soc. 38 (2018) 1829–1835, https://doi.org/10.1016/j.jeurceramsoc.2017.11.006.

[69] V.J. Keast, D.B. Williams, Quantification of boundary segregation in the analytical electron microscope, J. Microsc. 199 (2000) 45–55, https://doi.org/10.1046/j.1365-2818.2000.00694.x.

[70] J.C.C. Abrantes, J.A. Labrincha, J.R. Frade, Applicability of the brick layer model to describe the grain boundary properties of strontium titanate ceramics, J. Eur. Ceram. Soc. 20 (2000) 1603–1609, https://doi.org/10.1016/S0955-2219(00)00022-4.

[71] J.E. Bauerle, Study of solid electrolyte polarization by a complex admittance method, J. Phys. Chem. Solids 30 (1969) 2657–2670, https://doi.org/10.1016/0022-3697(69)90039-0.

[72] J. Maier, Electrochemical investigation methods of ionic transport properties in solids, SSP 39–40 (1994) 35–60, https://doi.org/10.4028/www.scientific.net/SSP.39-40.35.

[73] J.T.S. Irvine, D.C. Sinclair, A.R. West, Electroceramics: characterization by impedance spectroscopy, Adv. Mater. 2 (1990) 132–138, https://doi.org/10.1002/adma.19900020304.

[74] S. Rodewald, J. Fleig, J. Maier, Microcontact impedance spectroscopy at single grain boundaries in Fe-doped $SrTiO_3$ polycrystals, J. Am. Ceram. Soc. 84 (2001) 521–530, https://doi.org/10.1111/j.1151-2916.2001.tb00693.x.

[75] P. Balaya, J. Jamnik, J. Fleig, J. Maier, Mesoscopic electrical conduction in nanocrystalline $SrTiO_3$, Appl. Phys. Lett. 88 (2006) 062109, https://doi.org/10.1063/1.2171798.

[76] M. Vollman, R. Waser, Grain boundary defect chemistry of acceptor-doped titanates: space charge layer width, J. Am. Ceram. Soc. 77 (1994) 235–243, https://doi.org/10.1111/j.1151-2916.1994.tb06983.x.

[77] T. Bieger, H. Yugami, N. Nicoloso, J. Maier, R. Waser, Optical absorption relaxation applied to $SrTiO_3$ and ZrO_2: An in-situ method to study trapping effects on chemical diffusion, Solid State Ion. 72 (1994) 41–46, https://doi.org/10.1016/0167-2738(94)90122-8.

[78] F. Gunkel, R. Waser, A.H.H. Ramadan, R.A. De Souza, S. Hoffmann-Eifert, R. Dittmann, Space charges and defect concentration profiles at complex oxide interfaces, Phys. Rev. B 93 (2016) 245431, https://doi.org/10.1103/PhysRevB.93.245431.
[79] R. Moos, K.H. Härdtl, Dependence of the Intrinsic Conductivity Minimum of $SrTiO_3$ Ceramics on the Sintering Atmosphere, J. Am. Ceram. Soc. 78 (1995) 2569–2571, https://doi.org/10.1111/j.1151-2916.1995.tb08707.x.
[80] J. Fleig, The influence of non-ideal microstructures on the analysis of grain boundary impedances, Solid State Ion. 131 (2000) 117–127, https://doi.org/10.1016/S0167-2738(00)00627-5.
[81] J.-H. Hwang, K.D. Johnson, T.O. Mason, V.P. Dravid, Single grain boundary characterization of Nb-doped $SrTiO_3$ bicrystals using ac four-point impedance spectroscopy, Appl. Phys. Lett. 76 (2000) 2621–2623, https://doi.org/10.1063/1.126428.
[82] S.-H. Kim, J.-H. Moon, J.-H. Park, J.-G. Park, Y. Kim, Analysis of defect formation in Nb-doped $SrTiO_3$ by impedance spectroscopy, J. Mater. Res. 16 (2001) 192–196, https://doi.org/10.1557/JMR.2001.0031.
[83] S.-H. Kim, H.-T. Kim, J.-H. Park, Y. Kim, I-V characteristics and impedance spectroscopy of a single grain boundary in Nb-doped SrTiO3, Mater. Res. Bull. 34 (1999) 415–423, https://doi.org/10.1016/S0025-5408(99)00019-7.
[84] M.P. Zahler, D. Jennings, M. Kindelmann, O. Guillon, W. Rheinheimer, Reactive FAST/SPS sintering of strontium titanate as a tool for grain boundary engineering, J. Eur. Ceram. Soc. 43 (2023) 6925–6933, https://doi.org/10.1016/j.jeurceramsoc.2023.07.021.
[85] N. Wilcox, V. Ravikumar, R.P. Rodrigues, V.P. Dravid, M. Vollmann, R. Waser, K. K. Soni, A.G. Adriaens, Investigation of grain boundary segregation in acceptor and donor doped strontium titanate, Solid State Ion. 75 (1995) 127–136, https://doi.org/10.1016/0167-2738(94)00221-D.
[86] D. Jennings, M.P. Zahler, D. Wang, Q. Ma, W. Deibert, M. Kindelmann, C. Kübel, S. Baumann, O. Guillon, J. Mayer, W. Rheinheimer, Grain boundary segregation in iron doped strontium titanate: From dilute to concentrated solid solutions, Acta Mater. 273 (2024) 119941, https://doi.org/10.1016/j.actamat.2024.119941.
[87] A.L. Usler, R.A. De Souza, A critical examination of the Mott–Schottky model of grain-boundary space-charge layers in oxide-ion conductors, J. Electrochem. Soc. 168 (2021) 056504, https://doi.org/10.1149/1945-7111/abfb37.
[88] A.L. Usler, F. Ketter, R.A. De Souza, How space-charge behaviour at grain boundaries in electroceramic oxides is modified by two restricted equilibria, Phys. Chem. Chem. Phys. 26 (2024) 8287–8298, https://doi.org/10.1039/D3CP05870K.
[89] S.-J. Shih, S. Lozano-Perez, D.J.H. Cockayne, Investigation of grain boundaries for abnormal grain growth in polycrystalline $SrTiO_3$, J. Mater. Res. 25 (2010) 260–265, https://doi.org/10.1557/JMR.2010.0046.
[90] M. Bäurer, S.-J. Shih, C. Bishop, M.P. Harmer, D. Cockayne, M.J. Hoffmann, Abnormal grain growth in undoped strontium and barium titanate, Acta Mater. 58 (2010) 290–300, https://doi.org/10.1016/j.actamat.2009.09.007.
[91] S.H. Yoon, H. Kim, Experimental evidence for space charge segregation in Nb-doped $BaTiO_3$, J. Mater. Res. 16 (2001) 1479–1486, https://doi.org/10.1557/JMR.2001.0206.
[92] S.-Y. Chung, S.-J.L. Kang, V.P. Dravid, Effect of sintering atmosphere on grain boundary segregation and grain growth in niobium-doped $SrTiO_3$, J. Am. Ceram. Soc. 85 (2004) 2805–2810, https://doi.org/10.1111/j.1151-2916.2002.tb00532.x.
[93] J.G. Fisher, S.J.L. Kang, Nonlinear Migration of Faceted Boundaries and Nonstationary Grain Growth in Ceramics, MSF 715–716 (2012) 719–724, https://doi.org/10.4028/www.scientific.net/MSF.715-716.719.
[94] H. Sternlicht, W. Rheinheimer, A. Mehlmann, A. Rothschild, M.J. Hoffmann, W. D. Kaplan, The mechanism of grain growth at general grain boundaries in SrTiO3, Scr. Mater. 188 (2020) 206–211, https://doi.org/10.1016/j.scriptamat.2020.07.015.
[95] H. Sternlicht, W. Rheinheimer, J. Kim, E. Liberti, A.I. Kirkland, M.J. Hoffmann, W. D. Kaplan, Characterization of grain boundary disconnections in $SrTiO_3$ Part II: the influence of superimposed disconnections on image analysis, J. Mater. Sci. 54 (2019) 3710–3725, https://doi.org/10.1007/s10853-018-3095-5.
[96] H. Sternlicht, W. Rheinheimer, R.E. Dunin-Borkowski, M.J. Hoffmann, W. D. Kaplan, Characterization of grain boundary disconnections in $SrTiO_3$ part I: the dislocation component of grain boundary disconnections, J. Mater. Sci. 54 (2019) 3694–3709, https://doi.org/10.1007/s10853-018-3096-4.
[97] J. Han, S.L. Thomas, D.J. Srolovitz, Grain-boundary kinetics: a unified approach, Prog. Mater. Sci. 98 (2018) 386–476, https://doi.org/10.1016/j.pmatsci.2018.05.004.